metals

MDPI

Article

Defect Thermodynamics and the Intrinsic Stability Window of Mg_3Sb_2

Madhuri Birare [1], Adam Dębski [2], Władysław Gąsior [2] and Wojciech Gierlotka [1,*]

[1] Department of Materials Science and Engineering, National Dong Hwa University, Hualien 974, Taiwan; 811022204@gms.ndhu.edu.tw
[2] Institute of Metallurgy and Materials Science, Polish Academy of Science, 31-018 Krakow, Poland; debski.a@imim.pl (A.D.); gasior.w@imim.pl (W.G.)
* Correspondence: wojtek@gms.ndhu.edu.tw

Abstract

Magnesium antimonide (Mg_3Sb_2) has emerged as a promising high-performance thermoelectric material, yet its efficiency is fundamentally determined by intrinsic point defects. In this study, we present a comprehensive investigation of defects in the intermetallic compound Mg_3Sb_2 using first laws of thermodynamics and density functional theory (DFT) within the generalized gradient approximation (GGA). By calculating the energy of defect formation and the charge transition energy between energy levels, it was determined how the change in chemical potential associated with phase synthesis affects the phase stability and carrier concentrations. Calculations show that donor defects dominate in Mg-rich alloys, primarily antimony vacancies and magnesium atoms in interstitial positions. This means that in a phase with a slight magnesium excess, e.g., $Mg_{3.01}Sb_{1.99}$ at 1400 K, n-type conductivity dominates. In the opposite case, i.e., in an Sb-rich alloy, magnesium vacancies spontaneously form in the Wyckoff 1a position. These ionized acceptors induce strong self-compensation, blocking the Fermi level about 0.38 eV above the valence band maximum. As a result of this process, the Mg_3Sb_2 phase, at elevated temperatures, becomes the non-stoichiometric $Mg_{2.99}Sb_{2.01}$ phase, which causes the material to retain p-type conductivity and actively block doping-induced n-type conductivity. The conducted studies demonstrate that the homogeneity range of the Mg-Sb system, although traditionally considered narrow, has a significant impact on the semiconducting properties of the material. Furthermore, they also point to the need for continued research on high temperature in the area of synthetic defect engineering, interface engineering, and optimization of the thermoelectric properties of materials based on Mg-Sb alloys.

Keywords: thermoelectic material; ab initio; magnesium alloy; electronic structure

Check for updates

Academic Editor: Jan Vrestal

Received: 17 March 2026
Revised: 4 May 2026
Accepted: 6 May 2026
Published: 20 May 2026

Copyright: © 2026 by the authors. Licensee MDPI, Basel, Switzerland. This article is an open access article distributed under the terms and conditions of the Creative Commons Attribution (CC BY) license.

1. Introduction

The escalating global demand for sustainable energy solutions has driven extensive research into novel waste-heat recovery technologies. Thermoelectric materials are a critical focus of this research because they can directly convert heat into electricity and vice versa [1]. Operating entirely without moving parts or working fluids, they are highly attractive for energy harvesting and solid-state cooling applications [2]. Among the various candidates, magnesium antimonide (Mg_3Sb_2) has attracted considerable attention [3].

Mg_3Sb_2 is a Zintl-phase intermetallic compound celebrated for its outstanding thermoelectric properties and earth-abundant constituents. It crystallizes in a layered $CaAl_2Si_2$-type trigonal structure (space group P-3m1) and features a distinct bonding environment

where electropositive Mg atoms donate electrons to form covalently bonded Sb layers. This unique structural and electronic configuration yields a favorable combination of robust electronic transport properties and intrinsically low lattice thermal conductivity. Its multivalley conduction band and high carrier mobility lead to enhanced Seebeck coefficients and power factors, particularly in n-type compositions. Consequently, Mg_3Sb_2-based compounds have emerged as highly promising materials for mid-temperature-range applications (300–800 K) [4]. Through compositional tuning, alloying, and defect engineering, optimized n-type systems have achieved figure of merit (zT) values approaching or exceeding 2.0. Beyond its remarkable performance, Mg_3Sb_2 offers substantial sustainability advantages, utilizing relatively abundant and non-toxic elements compared to conventional materials like PbTe and Bi_2Te_3.

Fundamentally, the thermoelectric performance of Mg_3Sb_2 is governed by intrinsic point defects, including vacancies, interstitials, and antisite defects [5]. These structural imperfections dictate charge carrier scattering, profoundly influencing the material's electrical conductivity and overall transport properties. The stability and concentration of these native defects are highly sensitive to synthesis conditions, particularly temperature and chemical environment [6]. Because even subtle variations in defect density or type can trigger dramatic shifts in the macroscopic transport behavior, a precise understanding of the defect formation is essential for optimizing performance.

However, experimentally characterizing these imperfections at the atomic scale poses significant challenges. Conventional imaging techniques lack the necessary resolution [7], and advanced methods such as synchrotron X-ray diffraction and neutron scattering provide valuable insights but often struggle to accurately quantify defect concentrations or distinguish between specific defect types [8]. Furthermore, complex interactions between multiple defect species can complicate data interpretation.

To overcome these limitations, theoretical modeling has become an indispensable tool. First-principles calculations, particularly density functional theory (DFT) [9], enable the precise prediction of defect formation energies, stable charge states, and their impact on the electronic structure. By manipulating chemical potentials within the computational framework, DFT allows researchers to simulate various synthesis environments and isolate the behavior of individual charged defects—insights that are notoriously difficult to extract directly from experiments.

Although previous studies have focused on the formation energies of native point defects in Mg_3Sb_2, a comprehensive thermodynamic framework directly connecting defect chemistry with specific synthesis conditions and phase stability remains lacking. To bridge this gap, the present work integrates first-principles calculations with experimental findings to explain how intrinsic defects evolve across the homogeneity range of Mg_3Sb_2. We systematically investigate defect formation in two typical alloys: Mg-rich/Sb-poor and Sb-rich/Mg-poor. This approach provides a rigorous quantitative assessment of defect formation energies, stable charge states, and thermodynamic transition levels within the band gap. By delineating the thermodynamically accessible composition range, this study offers direct insights into defect concentrations at specific stoichiometries, establishing the key structure–property relationships necessary to guide material synthesis, control phase stability, and further boost the thermoelectric performance of Mg_3Sb_2 phase.

As recent research shows, the Mg_3Sb_2 phase has demonstrated strong potential for thermoelectric applications, as, for example, indium doping combined with structural engineering has enabled the achievement of a high thermoelectric figure of merit, ZT, reaching values as high as 2 [10]. Mohanty et al. [11] investigated the thermoelectric properties of this phase by optimizing the Mg excess. They confirmed that Mg vacancies are the dominant acceptor defects, leading to intrinsic p-type behavior, while Mg interstitials act as

compensating donor defects in n-type samples. However, the coexistence of these defects introduces significant structural disorder, which has been shown to enhance carrier scattering and localization effects, thereby reducing electron mobility. Similarly, Liang et al. [12] demonstrated that the thermal stability of n-type Mg_3Sb_2 is strongly influenced by the formation of Mg vacancies, which arise from the loss of magnesium atoms at elevated temperatures. Considering these findings from the literature, as well as the strong predictive capability of computational methods, it was decided to evaluate the thermoelectric properties of Mg_3Sb_2 influenced solely by native defects.

2. Computational Methods

First-principles calculations based on density functional theory (DFT) were performed using the Vienna Ab initio Simulation Package (VASP, version 6.4.1) [13]. The ion-electron interactions were described using the projector augmented-wave (PAW) method, while the exchange-correlation energy was treated within the generalized gradient approximation (GGA) parameterized by Perdew, Burke, and Ernzerhof (PBE) [14]. To ensure high accuracy in predicting the electronic properties, the Heyd–Scuseria–Ernzerhof (HSE06) hybrid functional was employed alongside the inclusion of spin–orbit coupling (SOC) effects.

Prior to the primary calculations, convergence tests for the plane-wave cutoff energy and k-point mesh density were conducted to ensure that the total energy was converged to within 2 meV per atom. Based on these tests, a cutoff energy of 350 eV and a k-point grid density of 0.1 A^{-1} were selected and maintained throughout this work. The primitive unit cell was first optimized using a strict electronic convergence criterion of 10^{-6} eV and an ionic force threshold of 0.01 eV/A. Additionally, the ADDGRID = .TRUE. tag was employed to enhance the grid resolution for the evaluation of augmentation charges.

Using the optimized lattice parameters, both pristine and defected supercells were constructed with the aid of the doped Python package doped 3.2.1 [15]. The size of the supercell $2 \times 2 \times 2$ which includes 50 atoms was suggested by the doped package [15] as a reasonable balance between size and computational cost. During the defect energy calculations, the internal atomic positions were fully relaxed, while the size and shape of the supercells were fixed to those of the pristine cell. To evaluate the defect formation energies under specific synthesis conditions, the total energies of the pure bulk Mg and Sb elemental phases were also calculated. Thermodynamic equilibrium of the compound requires the chemical potentials (μ_i) to satisfy the relation $3\mu_{Mg} + 2\mu_{Sb} = \mu_{Mg3Sb2}$. Consequently, under Mg-rich (Sb-poor) conditions, the chemical potential of Mg is constrained by the precipitation of its pure elemental phase ($\mu_{Mg} = \mu_{Mgbulk}$), with μ_{Sb} subsequently determined by the equilibrium condition. Conversely, under Sb-rich (Mg-poor) conditions, the antimony chemical potential is fixed by its bulk phase ($\mu_{Sb} = \mu_{Sbbulk}$). The chemical potentials chosen for the Mg-rich and Sb-rich limits imply that they are in thermodynamic equilibrium with their respective elemental bulk phases. Unlike metallic systems where non-stoichiometry is often accommodated by constitutional defects within a single phase, the zero-crossing of defect formation energies here signifies a transition where the secondary elemental phases become more stable than the defected host lattice, effectively pinning the Fermi level at the phase boundary.

Having calculated energies of pristine Mg_3Sb_2 and pure Mg and Sb, it is possible to calculate the formation energy of the intermetallic compound according to Equation (1):

$$\Delta E^0 = {E^0}_{Mg3Sb2} - (3/5){E^0}_{Mg} - (2/5){E^0}_{Sb} \quad (1)$$

where ΔE^0 is the formation energy of Mg_3Sb_2 per atom, ${E^0}_{Mg3Sb2}$ is the ab initio energy of Mg_3Sb_2 per atom and ${E^0}_{Mg}$ and ${E^0}_{Sb}$ are the energies of Mg and Sb in their stable reference states per atom, respectively.

The formation energy of a native defect in a charge state q was calculated using a well-known Zhang–Northrup formula given by Equation (2):

$$\Delta E = E(D^q) - E_{bulk} + \sum_i n_i \mu_i + q(E_{vbm} + E_F) + E_{corr} \quad (2)$$

where $E(D^q)$ is the total energy of a supercell containing a defect in charge state q, and E_{bulk} is the total energy of a pristine bulk supercell of the same size. The integer n_i represents the number of atoms of type i (host or impurity) that have been added to or removed from the supercell to create the defect, and μ_i is the corresponding chemical potential of those species.

The electronic contribution to the formation energy is captured by the term $q(E_{vbm} + E_F)$, where E_{vbm} is the absolute energy of the valence band maximum (VBM) of the bulk system, and E_F is the Fermi level referenced to the VBM (ranging from 0 to the band gap E_g). By referencing E_F to the VBM, the formation energy becomes independent of the arbitrary zero of the energy scale. Finally, E_{corr} is a correction term that accounts for finite-size effects in supercell calculations, including point sampling for shallow impurities and electrostatic or elastic interactions between periodic images of the defects.

The change in Fermi energy was calculated assuming a dilute defect concentration, where defect–defect interactions are neglected. In this situation, the density of free charge carriers is controlled directly by the capacity of charged defects to either donate electrons from or donate electrons to the conduction and valence bands. The defect and charge carrier equilibrium concentration should fulfill the charge neutrality requirement, so that the net number balance between positive and negative charges in the system is maintained. This constrained can be expressed mathematically as shown below.

$$n - p = \sum_d q_d c_{q,d} \quad (3)$$

where n is a free electron concentration in the conduction band, p is a free hole concentration in the valence band, q_d is the charge state of defect d, and, finally, $c_{q,d}$ is a concentration of defect d which is given by Boltzmann's distribution in the dilute limit of concentration m

$$c_{d,q} = c_o e \frac{-\Delta \mathrm{Hd,q}}{\mathrm{kT}} \quad (4)$$

where k is Boltzmann's constant, c_o is the concentration of possible defect sites in the cell, and $\Delta H_{d,q}$ is the formation enthalpy of a given defect.

The carrier concentrations n and p are given by the following Equations (5a) and (5b), respectively:

$$n = \sum_{ECBM}^{+\infty} n(E) f(\mathrm{E}, \mu_e, \mathrm{T}) \mathrm{dE} \quad (5a)$$

$$p = \sum_{k=0}^{EVBM} n(E)[1 - f(\mathrm{E}, \mu_e, \mathrm{T})] \mathrm{dE} \quad (5b)$$

where $n(E)$ is the density of states of a perfect crystal and $f(E,\mu_e,T)$ is the Fermi–Dirac distribution.

Assuming a non-degenerate limit where the Fermi levels are more than several kT below the CBM and several kT above VBM, the carrier concentrations can be simplified [16] to

$$\mathrm{n} = \mathrm{N_C} \exp\left(-\frac{ECBM - \mu e}{kT}\right) \quad (6a)$$

$$\mathrm{p} = \mathrm{N_v} \exp\left(-\frac{\mu e - EVBM}{kT}\right) \quad (6b)$$

where E_{VBM} and E_{CBM} are the energies of the valence band maximum and conduction band minimum, respectively; N_C and N_V are the effective densities of states in the conduction and valence bands, respectively, and they are given as follows:

$$N_C = 2\left(\frac{2\pi m_e^* kT}{h^2}\right)^{\frac{3}{2}} \quad (7a)$$

$$N_V = 2\left(\frac{2\pi m_h^* kT}{h^2}\right)^{\frac{3}{2}} \quad (7b)$$

where m_e and m_h are the effective masses of electrons and holes, respectively.

To overview the intrinsic homogeneity range of Mg_3Sb_2, equilibrium point defect concentrations were calculated from first-principles defect formation energies. The equilibrium concentration of each defect D^q in charge state q was obtained using Boltzmann statistics:

$$C(D^q) = N_{sites} \exp\left(\frac{\Delta H_{f(D^q)}}{k_B T}\right), \quad (8)$$

where N_{sites} is represented by the number of available lattice sites, ΔH_f (D^q) is the defect formation energy, k_B is the Boltzmann constant, and T is the temperature.

The Fermi level was determined by enforcing overall charge neutrality. The deviation from ideal stoichiometry was derived from summing the contributions of all intrinsic defects proportional to their respective change in elemental composition.

$$\Delta x_i = \sum_D n_i(D)C(D), \quad (9)$$

where n_i(D) is the number of atoms of element *i* added or removed per defect.

This approach recognizes direct quantification of the compositional deviation from ideal Mg_3Sb_2 stoichiometry arising from intrinsic defect equilibria.

Moreover, since the Mg_3Sb_2 phase is a potential thermoelectric (TE) material, it is possible to theoretically predict TE properties, such as Seebeck coefficient or electrical conductivity. This kind of calculation requires additional information, such as the elasticity matrix, high-frequency dielectric constant, and static dielectric constant. However, it must be emphasized that the calculations do not take into account grain boundaries that significantly affect TE properties.

The Hessian matrix with elements of the stiffness tensor C_{ij} necessary for the generalized Hook's law, which in the Voigt notation [17] can be written as follows:

$$\begin{bmatrix} \sigma_1 \\ \sigma_2 \\ \sigma_3 \\ \tau_1 \\ \tau_2 \\ \tau_3 \end{bmatrix} = \begin{bmatrix} C_{11} & C_{12} & C_{13} & 0 & 0 & 0 \\ C_{21} & C_{22} & C_{23} & 0 & 0 & 0 \\ C_{31} & C_{32} & C_{33} & 0 & 0 & 0 \\ 0 & 0 & 0 & C_{44} & 0 & 0 \\ 0 & 0 & 0 & 0 & C_{55} & 0 \\ 0 & 0 & 0 & 0 & 0 & C_{66} \end{bmatrix} \begin{bmatrix} \varepsilon_1 \\ \varepsilon_2 \\ \varepsilon_3 \\ \gamma_1 \\ \gamma_2 \\ \gamma_3 \end{bmatrix} \quad (10)$$

where i, j = 1…6, C_{ij} is the element of the second-order stiffness tensor, σ_i and τ_1 are the normal and shear stress responses of the solid to external loading and ε_i and γ_i are the normal and shear strains, respectively.

The most important task for the calculation of the different mechanical properties of materials is to obtain the elements of the stiffness tensor in Equation (10) because, in such cases, determinations of various elastic properties is necessary to calculate of TE properties using the AMSET [18] code. Moreover, having the stiffness tensor it is possible to determine various mechanical properties, such as bulk and shear moduli or Poisson's ratio. In order to

achieve this goal, the Nielsen and Martin [19] approach was applied for the determination of C_{ij} elements in Equation (10), and, in the case of polycrystalline materials, thought to be quasi-isotropic, the approaches of Voigt [17] concerning bounds for the isostrain and Reuss [20] for bounds of the isostress were accepted. Because the Voight method predicts lower values than the Reuss method, an approach called the Voigt–Reuss–Hill (VRH) approach, which gives the average values of mechanical properties, was found to be the best one.

The Voigt bounds are given as follows:

$$\begin{cases} 9K_V = (C_{11} + C_{22} + C_{33}) + 2(C_{12} + C_{23} + C_{31}) \\ 15G_V = (C_{11} + C_{22} + C_{33}) - (C_{12} + C_{23} + C_{31}) + 4(C_{44} + C_{55} + C_{66}) \end{cases} \quad (11)$$

The Reuss bounds are expressed as:

$$\begin{cases} 1/K_R = (S_{11} + S_{22} + S_{33}) + 2(S_{12} + S_{23} + S_{31}) \\ 15/G_R = 4(S_{11} + S_{22} + S_{33}) - 4(S_{12} + S_{23} + S_{31}) + 3(S_{44} + S_{55} + S_{66}) \end{cases} \quad (12)$$

where $S_{ij} = C_{ij}^{-1}$ is the elastic compliance tensor, K is the bulk modulus and G is the shear modulus. The VRH approach defines the bulk (K_{VRK}) and shear (G_{VRK}) moduli according to the following relations:

$$K_{VRK} = 0.5(K_V + K_R) \quad (13)$$

$$G_{VRK} = 0.5(G_V + G_R) \quad (14)$$

Moreover, based on the obtained bulk and shear moduli (Equations (13) and (14)), Young's modulus E and Poisson's ratio ν can also be calculated with the use of the following equations:

$$E = \frac{9KG}{3K + G} \quad (15)$$

$$\nu = \frac{3K - 2G}{2(3K + G)} \quad (16)$$

Because hardness is also an important mechanical property of materials, its modeled theoretical values are very interesting for researchers engaged in the use and development of new materials for the industry and also for economic reasons. In this work, the hardness of intermetallic phases were modeled based on two different equations available in the literature. Both are based on the values of the bulk and shear moduli. The first equation, proposed by Chen et al. [21], assumes that the Vicker's hardness is given as follows:

$$H_V = 2\left[\left(\frac{G}{B}\right)^2 G\right]^{0.585} - 3 \quad (17)$$

where H_V is the Vicker's hardness and G and B = K_{VRK} are the shear and bulk moduli given in GPa, respectively.

The second equation, being a modification of Equation (17), was given by Tian et al. [22] as the conclusion of discussion on the influence of electronegativity and bonding strength on Vicker's hardness. The proposed relation is shown below:

$$H_V = 0.92\left(\frac{G}{B}\right)^{1.137} G^{0.708} \quad (18)$$

All the symbols in Equation (18) have the same meanings as in Equation (17).

Because, as it is known from the literature and our earlier study [23], the Vicker's hardness values calculated with the use of Equations (17) and (18) sometimes differ substantially from each other, both results will be shown in this work.

Another information necessary for the calculation of the TE properties are high-frequency and static dielectric constants.

The static dielectric constant is defined as the zero-frequency limit of the dielectric function:

$$\varepsilon_S = \lim_{\omega \to 0} \varepsilon(\omega) \tag{19}$$

where ε_S is the static dielectric constant, $\varepsilon(\omega)$ is the complex, frequency-dependent dielectric function, and ω is the angular frequency of the applied electric field in rad/s.

The static dielectric function corresponds to the full equilibrium response of the system under a slowly varying or static external electric field. This function can be expressed as a sum of the ionic, electronic, and dipole contributions reflecting the cumulative screening effect arising from all accessible degrees of freedom.

In contrast, the high-frequency dielectric constant is defined in the limit of sufficiently large frequencies:

$$\varepsilon_\infty = \lim_{\omega \to \infty} \varepsilon(\omega) \tag{20}$$

where slower polarization processes, such as ionic motion and dipolar reorientation, are unable to follow the rapidly oscillating field.

The above-mentioned properties, along with density of states of the Mg_3Sb_2 phase, were used in AMSET [18] code to calculate the Seebeck coefficient, electrical conductivity, and electronic thermal conductivity. However, the thermoelectric efficiency of a material is commonly evaluated using the dimensionless figure of merit:

$$ZT = \frac{S^2 \delta T}{\kappa_e + \kappa_L} \tag{21}$$

where ZT is the figure of merit, S is the Seebeck coefficient, δ is the electrical conductivity, κ_e is the electronic thermal conductivity, κ_L is the lattice thermal conductivity, and T is the absolute temperature.

The lattice thermal conductivity was calculated using Phonopy [24] and Phono3py [24] codes. The lattice thermal conductivity arises from heat transport by phonons and is obtained by solving the Boltzmann phonon transport equation (BTE) using the single-mode relaxation time approximation. Within this framework, the lattice thermal conductivity tensor is expressed by the following equation:

$$\kappa_{\alpha\beta} = \frac{1}{V} \sum\nolimits_{\lambda} C_\lambda \, v_{\lambda,\alpha} \, v_{\lambda,\beta} \, \tau_\lambda \tag{22}$$

where C_λ is the mode heat capacity, v_λ is the phonon group velocity, and τ_λ is the phonon lifetime.

In this work, second-order interatomic force constants (IFCs) were calculated using the finite displacement method as implemented in Phonopy [24], providing harmonic phonon properties such as phonon frequencies and group velocities. Third-order IFCs, which describe anharmonic phonon–phonon interactions responsible for scattering processes, were computed using Phono3py [24]. The phonon lifetimes obtained from these anharmonic interactions, combined with harmonic properties from Phonopy, were then used to evaluate the lattice thermal conductivity by numerically solving the BTE and the results obtained from AMSET [18] and Phono3py [24] codes were finally applied in Equation (21) to calculate thermoelectric figure of merit of the Mg_3Sb_2 phase.

3. Results and Discussion

As a preliminary step, the formation energy of the Mg_3Sb_2 phase was calculated and compared with the existing literature. Although these values are readily available, this comparison served as a baseline validation of our computational approach. The formation energy calculated in this work was −0.35 eV/atom (−34,048 J/mol-atom), which is in excellent agreement with the Materials Project value of −0.364 eV/atom [25,26]. However, it is lower in magnitude than the −0.622 eV/atom reported in the OQMD [27,28]. Furthermore, the optimized lattice parameters were calculated to be $a = b = 4.5966$ Å and $c = 7.2633$ Å. These dimensions align closely with experimental determinations of $a = b = 4.573$ Å, $c = 7.229$ Å [29] and $a = b = 4.5636$ Å, $c = 7.228$ Å [30].

The indirect bandgap of the intermetallic compound Mg_3Sb_2 was calculated to be 0.654 eV, which is in excellent agreement with the 0.6 eV reported in the literature [31].

The valence band maximum (VBM) and conduction band minimum (CBM) were determined to be 4.123 eV and 4.778 eV, respectively. These absolute band edge positions establish the Fermi level range employed during our defect formation energy evaluations, and they align well with earlier theoretical predictions for Mg-containing Zintl phases [9].

First-principles studies of Mg_3Sb_2 have reported similar indirect bandgaps ranging from 0.41 eV to 0.65 eV, depending on the specific exchange-correlation approach utilized. This variation highlights the well-known tendency of semi-local DFT functionals to underestimate bandgaps relative to experimental values [32]. Furthermore, ab initio calculations consistently identify Mg_3Sb_2 as an indirect semiconductor with the VBM located at the Γ point and the CBM situated elsewhere within the Brillouin zone, which perfectly corroborates the theoretical band structures observed in this study [33].

Standard geometry optimization procedures often converge to metastable local minima or saddle point configurations, which can lead to inaccurate defect energetics, erroneous equilibrium defect concentrations, and incorrect charge transition levels. To mitigate these issues, all initial defect geometries were systematically perturbed by applying selective bond distortions and atomic vibrations to atoms near the defect, and the ground state geometry of every defect structure was thoroughly determined using the ShakeNbreak [32] code.

The resulting structures were then subjected to internal atomic relaxation, with the supercell shape and volume constrained to match those of the pristine lattice. Finally, the total energies obtained for each defective supercell were used to calculate the defect formation energies according to Equation (2) using the doped code [15]. These calculations were performed for the Mg_3Sb_2 phase enriched in both Mg and Sb, and the results are presented in Figure 1a,b. To account for random interactions arising from the finite size of the supercell, the thermodynamic charge-state transition levels were corrected using the Kumagai (eFNV) scheme. Because this correction relies on the dielectric screening of the material, the macroscopic dielectric tensor was computed independently. The calculated static relative dielectric constant of Mg_3Sb_2 was found to be 31.15.

An analysis of Figure 1a reveals that for Mg_3Sb_2 phase in Mg-rich growth conditions, the defect chemistry is highly dependent on the Fermi level. Near the valence band maximum, the dominant defect is the magnesium interstitial (Mg_i) in the +3 charge state, located at the C3v site. This position represents a high-symmetry environment, situated exactly along a three-fold rotational axis within the lattice. However, as the Fermi level (EF) increases to 0.38 eV, a thermodynamic transition occurs. Above this threshold, the magnesium vacancy (V_{Mg}) at the interlayer 1a Wyckoff position (in the −2 charge state) becomes the most dominant defect. Slightly more energetically demanding are the magnesium interstitial situated at the lower-symmetry Cs position, as well as the intralayer magnesium vacancy at the 2d Wyckoff position. The remaining native point defects require

significantly higher formation energies and are therefore less thermodynamically probable, as detailed in Figure 1a.

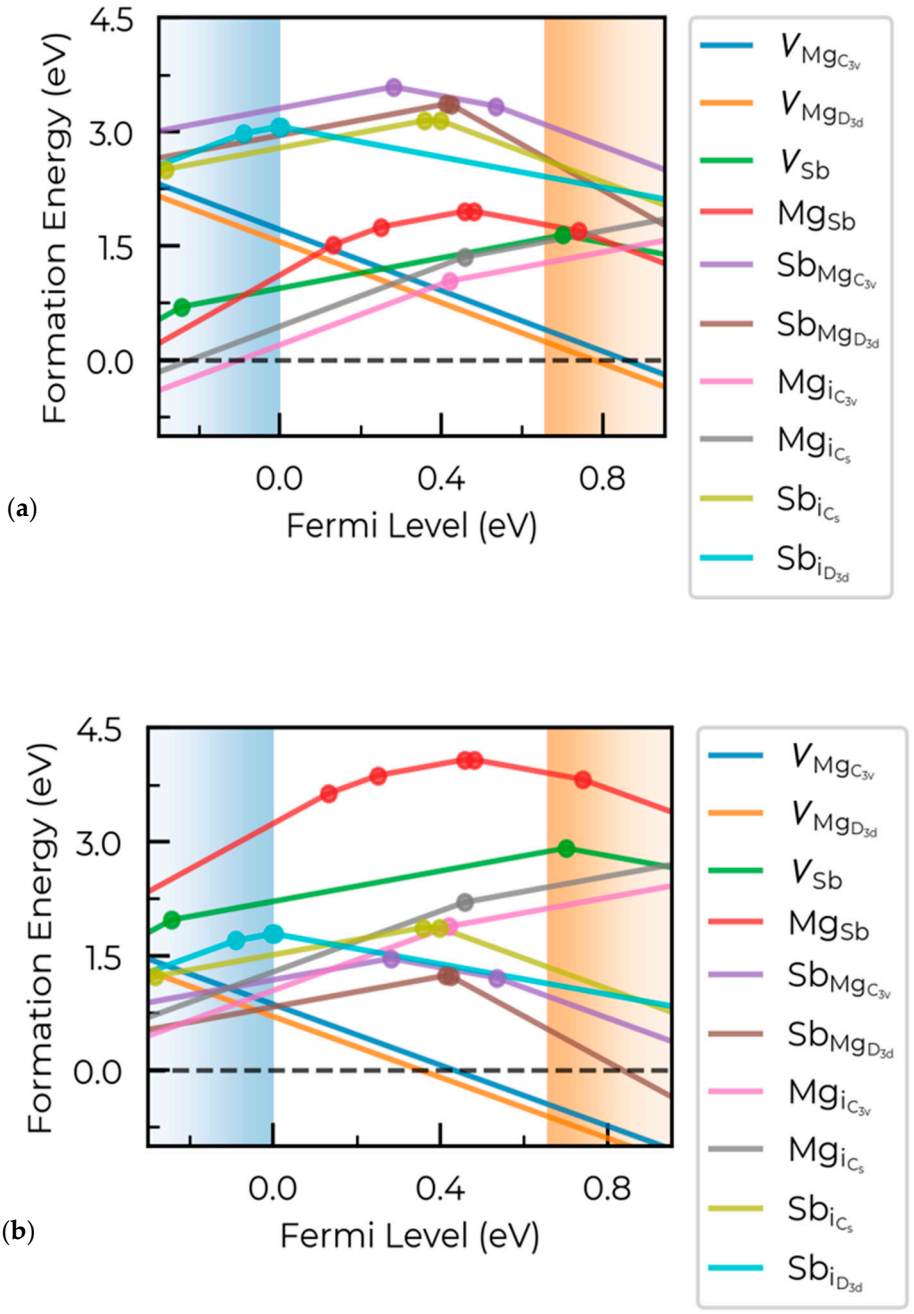

Figure 1. Calculated defect formation energies (ΔE) as a function of the Fermi level (E_F) for native point defects in Mg_3Sb_2. The two panels represent the extreme thermodynamic limits of the stability region: (**a**) Mg-rich (equilibrium with bulk Mg) and (**b**) Sb-rich (equilibrium with bulk Sb) growth conditions. In both panels, the Fermi level on the x-axis is referenced to the valence band maximum (VBM), where E_F = 0 eV. The shaded vertical region indicates the conduction band, with the band gap (E_g) separating the VBM from the CBM.

In the case of Mg_3Sb_2 phase enriched in Sb, the defect formation energy landscape shifts significantly. Our calculations indicate that the most thermodynamically favorable defect in this regime is the magnesium vacancy (V_{Mg}) located at the interlayer 1a Wyckoff position (D3d symmetry site). Notably, within the calculated fundamental band gap of 0.654 eV, the formation energy of this highly ionized vacancy (in the −3 charge state) exhibits a critical transition. As shown in Figure 1b, at an EF of approximately 0.38 eV

above the valence band maximum, the formation energy of this defect crosses from positive to negative values.

This thermodynamic zero-crossing has profound implications for the electronic properties and dopability of Mg_3Sb_2. From a physical point of view, a negative formation energy means that once the Fermi level is pushed above 0.38 eV—such as through intentional n-type doping attempts—the pristine crystal lattice becomes thermodynamically unstable. As a result, the material will spontaneously generate massive concentrations of 1a Mg vacancies to lower its overall system energy.

Because these magnesium vacancies act as deep electron acceptors, they immediately capture free electrons introduced by n-type dopants. This spontaneous defect generation creates a strong "self-compensation" effect. Ultimately, these vacancies pin the Fermi level at ∼0.38 eV, acting as a blocking thermodynamic force. This pinning mechanism demonstrates that achieving heavy n-type conductivity in Mg_3Sb_2 phase is impossible in the Sb-enriched sample. Therefore, studies on n-type electrical performance optimization should focus on the Mg-enriched phase.

The native defect formations obtained in this work show similar characteristics to those in recently published work by Ohno et al. [33], especially when the dominant defect is discussed.

The thermodynamic limits of dopability in Mg_3Sb_2 are determined by Fermi level and a self-compensation mechanism in which the spontaneous formation of native defects counteracts external doping. As the Fermi level (E_F) is pushed toward the conduction band, the formation energy of acceptor-like defects—most notably Magnesium vacancies (V_{Mg})—drops significantly. When these energies approach 0.0 eV, the lattice spontaneously creates vacancies that act as electron sinks, effectively trapping E_F and preventing further n-type conductivity. Conversely, as E_F shifts toward the valence band maximum, donor-like defects such as interstitials (Mg_i and Sb_i) become energetically favorable, donating electrons that annihilate holes and pin the Fermi level near the valence band edge. The variation between the two growth environments highlights the critical role of chemical potentials in defining these dopability windows. Under Mg-rich conditions (top plot, Figure 1a), Mg_3Sb_2 is in equilibrium with bulk Mg metal and in this case, the higher vacancies formation energy expands the available range of Fermi level, enabling more stable n-type characteristics. In the Sb-rich regime (bottom plot, Figure 1b), the system is in equilibrium with bulk Sb. The reduced formation energy of V_{Mg} in this environment causes the n-type pinning limit to move deeper into the band gap, severely restricting electron concentrations. Critically, these pinning limits represent phase stability boundaries and for a crystal to become intrinsically unstable, the zero-crossing of defect formation energies signifies a transition where the system favors the precipitation of elemental secondary phases (Mg or Sb) over the further incorporation of dopants into the single-phase host lattice.

As can be seen from Figure 1a,b, the most probable defects do not change their charge states within the hull inside the band gap. Under Mg-rich growth conditions, the interstitial Mg defect changes its charge from +3 to +2 inside the band gap; however, this change occurs outside the hull. The formation energies of other defects under Mg-rich conditions are significantly higher; therefore, their charge-state changes can be neglected in this discussion.

In the case of Sb-rich growth conditions, it can be observed that there is no change in charge states within the hull inside the band gap. Both of the most probable defects from an energetic point of view, namely $V_{\mathrm{Mg}}(D_{3d})$ and $V_{\mathrm{Mg}}(C_{3v})$, do not exhibit any change in charge state. The next most relevant defect, a substitution of Mg by Sb on the D_{3d} site, shows a change in charge from +1 to 0, and subsequently to -1 and -2 around the Fermi level $E_F = 0.4$ eV. It is noteworthy that this charge-state transition occurs very rapidly,

within just a few hundred meV. Other defects require higher formation energies, making their probability of occurrence very low, and thus they will not be discussed further here.

Figure 1a,b provide detailed information on charge-state transitions in close proximity to the energy gap for defects with reasonable formation energies, up to 4.5 eV. These figures can be used to extract further insights into the energetics and charge-state behavior of the defects.

The carrier concentration was examined as a function of temperature, with the Fermi level determined self-consistently at each point, as shown in Figure 2a,b. This analysis provides a clear understanding of how intrinsic point defects govern the electrical properties of the material under varying chemical potential limits.

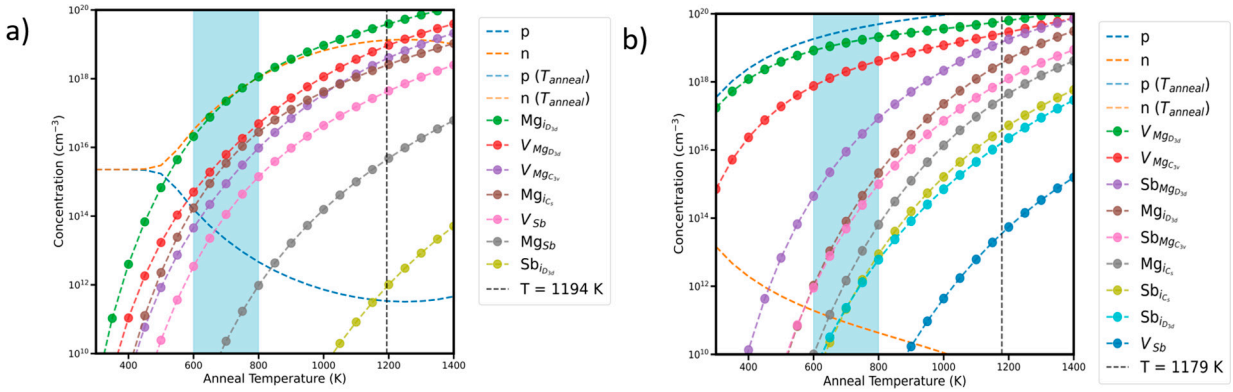

Figure 2. Defects and carrier concentrations as functions of temperature in (**a**) Mg-enriched and (**b**) Sb-enriched Mg_3Sb_2 phases.

In the Mg-rich regime (Figure 2a), magnesium interstitials (Mg_i) are the predominant donor defects. Their high concentration contributes free electrons to the conduction band, resulting in robust n-type conductivity across the intermediate and high-temperature ranges. While Sb vacancies (V_{Sb}) also act as donors, their concentration remains lower than that of Mg_i, making the magnesium interstitial the primary species responsible for the n-type behavior.

Conversely, in the Sb-rich regime (Figure 2b), magnesium vacancies (V_{Mg}) dominate the defect chemistry. These act as acceptors that generate holes in the valence band, thereby inducing p-type behavior. Other native defects, such as Mg and Sb antisites, possess significantly higher formation energies and occur at negligible concentrations, playing a minor role in overall carrier generation.

As temperature increases, defect concentrations rise following typical Arrhenius behavior. The stabilization or "leveling off" of carrier concentrations at extreme temperatures indicates that the system has reached the solubility limit. Beyond these points, as discussed regarding the chemical potential boundaries, the Mg_3Sb_2 phase is in equilibrium with bulk Mg or Sb, and further deviations in stoichiometry would lead to the precipitation of these secondary phases rather than a further increase in point defect concentration.

Ultimately, these results demonstrate that the intrinsic electrical behavior of Mg_3Sb_2 is highly tunable via synthesis conditions: Mg-rich conditions promote n-type conductivity through Mg_i formation, while Sb-rich conditions favor p-type conductivity dominated by V_{Mg}.

Furthermore, Figure 3 illustrates the calculated carrier concentration at temperatures 300 K and 875 K, providing deeper insight into the evolution of the electronic properties under extreme thermal conditions. As expected, the rising temperature drives a significant increase in the total number of thermally excited charge carriers. Specifically, there is a noticeable increase in the hole concentration associated with the valence band maximum

(VBM), while electrons dominate near the conduction band minimum (CBM). In light of these results, it is necessary to propose an improved thermodynamic description of the Mg-Sb system that accurately take into account the narrow homogeneity range suggested by the literature and theoretically confirmed in this work [34]. Although this homogeneity range may appear physically negligible, it exerts a profound influence on the semiconducting properties of the material. Our results indicate that while the effective Mg composition remains near ideal stoichiometry of the Mg_3Sb_2 phase, Mg vacancies increasingly dominate at elevated temperatures, driving the lattice into a moderately Mg-deficient state. Therefore, developing an improved thermodynamic model that captures these subtle, temperature-dependent non-stoichiometries is of great importance for optimizing this material for industrial applications.

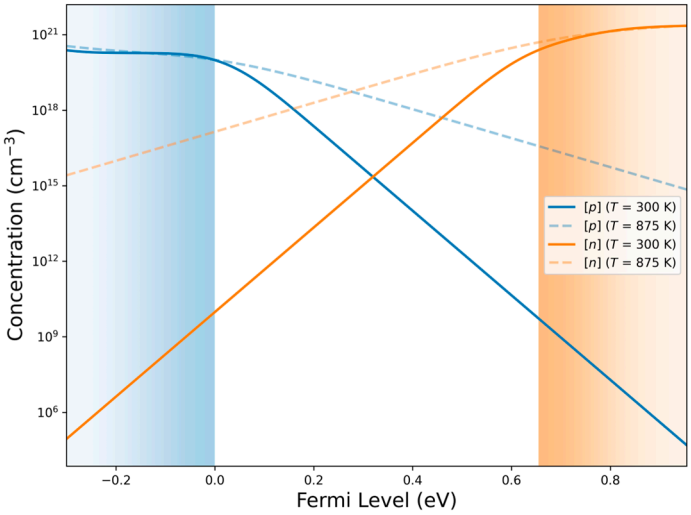

Figure 3. Variation in carrier concentrations through a band gap as a function of temperature.

To further quantify the temperature-dependent phase boundaries, the calculated intrinsic defect concentrations were used to determine the exact extent of off-stoichiometry within the Mg_3Sb_2 homogeneity range. In the case of higher Mg content, the concentration of interstitial magnesium at elevated temperatures varies drastically, ranging from approximately 10^{13} cm^{-3} at 400 K to 10^{20} cm^{-3} at 1400 K. Assuming that the lattice volume is independent of temperature, this defect accumulation physically shifts the solid solution toward a magnesium-excess state. The calculated effective stoichiometries at 400 K, 600 K, and 1400 K are Mg_3Sb_2, $Mg_{3.0000025}Sb_2$, and $Mg_{3.0186}Sb_2$, respectively. While the deviation at lower temperatures is virtually negligible, the accumulation of extra Mg atoms at high temperatures significantly expands the homogeneity range. For thermoelectric applications, this controlled Mg-excess is highly beneficial because the interstitial donors continuously provide free electrons to the conduction band, reinforcing the desired n-type conductivity without severely disrupting the crystal lattice or degrading carrier mobility.

Conversely, the structural response under Sb-rich synthesis conditions is markedly different, dominated by the heavy accumulation of magnesium vacancies and Sb-on-Mg antisite defects. Applying the same volumetric calculations, the non-stoichiometry shifts aggressively toward magnesium deficiency. At the corresponding temperatures of 400 K, 600 K, and 1400 K, the effective compositions are $Mg_{2.99984}Sb_2$, $Mg_{2.99879}Sb_2$, and a highly defective $Mg_{2.97161}Sb_{2.00077}$, respectively, which leads to a change in the phase boundary. The concentration calculations are consistent with the study by Ohno et al. [33] who showed that Mg_3Sb_2 behaves as a nearly linear compound. The Sb concentrations at different temperatures for the Mg_3Sb_2 phase enriched in Mg and Sb are gathered in Table 1.

Table 1. Equilibrium concentration of the Mg_3Sb_2 phase enriched in Mg and Sb.

T [K]	x_{Sb}	
	Mg-Rich Growth	**Sb-Rich Growth**
400	0.4	0.4000128
600	0.3999998	0.40009682
800	0.399988	0.40024935
1000	0.39989043	0.4005563
1200	0.39961158	0.40145506
1400	0.39851751	0.40237673

From a thermoelectric perspective, this pronounced structural degradation determines the material's fundamental limits. The immense concentration of Mg vacancies acts as a vast reservoir of hole-producing acceptors, rigidly confining the material into a p-type conductor and completely preventing any n-type doping. It should be noted that while a dense population of point defects in the $Mg_{2.94}Sb_{2.01}$ lattice can beneficially suppress lattice thermal conductivity via heightened phonon scattering, it also degrades electronic transport through strong charge carrier scattering. Ultimately, these calculations confirm that the "ideal" Mg_3Sb_2 crystal is a dynamic solid solution. Tailoring the growth conditions directly restricts the boundaries of this homogeneity range, which in turn strictly controls the final thermoelectric performance of the material.

As it was mentioned earlier, the calculation of TE properties requires information of elasticity matrix as well as static and high-frequency dielectric constant. The stiffness tensor matrix obtained in this work is shown below.

Based on the stiffness tensor matrix (Table 2), the average mechanical properties of the bulk Mg_3Sb_2 phase were calculated and are gathered in Table 3 below.

Table 2. Stiffness tensor matrix calculated in this work.

C_{ij}	1	2	3	4	5	6
1	72.454	36.672	20.975	−6.044	−0.002	0.000
2	36.672	72.453	20.978	6.044	0.000	0.000
3	20.975	20.978	77.282	0.000	0.000	0.000
4	−6.044	6.044	0.000	14.240	0.000	0.000
5	0.000	0.000	0.000	0.000	14.248	−6.048
6	0.000	0.000	0.000	0.000	−6.048	17.878

Table 3. Mechanicla properties of the Mg_3Sb_2 phase.

Mechanical Property	**Voigt**	**Reuss**	**Hill**
Bulk modulus B (GPa)	42.16	42.014	42.087
Young's modulus E (GPa)	49.21	40.807	45.058
Shear modulus G (GPa)	18.85	15.248	17.047
Poisson ratio	0.31	0.338	0.322
P-wave modulus (GPa)	67.29	62.345	64.816
Pugh's ratio (B/G)	2.24	2.755	2.269
Vicker's hardness (GPa) [21]	1.33	0.003	0.643
Vicker's hardness (GPa) [22]	2.94	2.00	2.452

The mechanical properties summarized in Table 3 exhibit the typical spread between the Voigt (upper bound), Reuss (lower bound), and Hill (Voigt–Reuss average) approximations, providing insight into the elastic behavior and anisotropy of the material.

The bulk modulus shows very close agreement among the three schemes, with values of $B_V = 42.16$ GPa, $B_R = 42.014$ GPa, and $B_H = 42.087$ GPa. The slight difference (<0.4%) indicates that the material exhibits minimal compressibility anisotropy and that the bulk response is highly isotropic. This suggests that the resistance to uniform volume change is well-defined and robust. In contrast, the shear modulus demonstrates a more noticeable spread, with $G_V = 18.85$ GPa, $G_R = 15.248$ GPa, and $G_H = 17.047$ GPa. The relative difference between Voigt and Reuss bounds (~19%) reflects moderate elastic anisotropy in shear deformation. Since shear response is more sensitive to directional bonding characteristics, this indicates non-uniform resistance to shape distortion at the microscopic level. A similar trend is observed for Young's modulus, where $E_V = 49.21$ GPa, $E_R = 40.807$ GPa, and $E_H = 45.058$ GPa. The spread (~17%) further supports the presence of anisotropy in the elastic stiffness, with the Hill average providing a reliable estimate for polycrystalline behavior. The Poisson ratio ranges from 0.31 to 0.338, with a Hill average of $\nu_H = 0.322$. This value is relatively high and typically associated with materials exhibiting significant central-force interactions and a degree of ductility. Values above ~0.26 often indicate metallic or ductile properties rather than brittle covalent networks. The P-wave modulus follows the expected trend, with $M_V = 67.29$ GPa, $M_R = 62.345$ GPa, and $M_H = 64.816$ GPa, again showing moderate anisotropy but consistent overall elastic behavior. An important indicator of ductility is the Pugh ratio, which yields values of 2.24 (Voigt), 2.755 (Reuss), and 2.269 (Hill). Since all values exceed the critical threshold of 1.75, the material can be classified as ductile. The Hill average ($B/G \approx 2.27$) suggests a good balance between resistance to fracture and plastic deformation. The estimated Vickers hardness values show significant variation depending on the empirical model used. Using the model from [21], the hardness ranges from 0.003 to 1.33 GPa, with a Hill average of 0.643 GPa, which appears unrealistically low and suggests that this model may not be well-suited for the present material system. In contrast, the model from [22] yields more physically reasonable values, with H_V ranging from 2.00 to 2.94 GPa and an average of 2.452 GPa. These values indicate that the material is relatively soft, consistently with its low shear modulus and high Pugh ratio.

Overall, the material can be characterized as mechanically soft, moderately anisotropic in shear and Young's modulus, and distinctly ductile. The close agreement in the bulk modulus confirms isotropic compressibility, while the deviations in shear-related properties highlight the directional dependence in bonding. The combination of low hardness and high B/G ratio suggests that this material is suitability for applications where deformability and fracture toughness are desired.

The calculated dielectric properties are gathered below in Tables 4 and 5a–c.

Table 4. High-frequency dielectric constant obtained in this work.

$\varepsilon_{\infty ij}$	**1**	**2**	**3**
1	15.48947	0.000044	0.000037
2	0.000044	15.48952	−0.000021
3	0.000037	−0.000021	17.486093
Average: 16.155028			

Table 5. (**a**) Electronic contribution of static dielectric constant obtained in this work. (**b**) Ionic contribution of static dielectric constant obtained in this work. (**c**) Static dielectric constant obtained in this work.

(**a**)			
ε_{0eij}	**1**	**2**	**3**
1	14.317291	0.00004	0.000034
2	0.00004	14.317337	−0.00002
3	0.000034	−0.00002	16.349224
Average: 14.994617			
(**b**)			
ε_{0iij}	**1**	**2**	**3**
1	16.709548	0.000047	0.000038
2	0.000047	16.709602	−0.000022
3	0.000038	−0.000022	17.375707
Average: 16.931619			
(**c**)			
ε_{0iij}	**1**	**2**	**3**
1	31.026839	0.000087	0.000072
2	0.000087	31.026939	−0.000042
3	0.000072	−0.000042	33.724931
Average: 31.926236			

The calculated dielectric properties show a consistent and physically meaningful picture of the polarization response, with a clear separation between electronic and ionic contributions and only weak anisotropy of the dielectric tensor.

The high-frequency dielectric tensor ε_∞, obtained from LOPTICS, is nearly diagonal with very small off-diagonal components ($< 10^{-4}$), indicating that the principal dielectric axes are well-aligned with the crystallographic axes and that cross-polarization effects are negligible. The diagonal components are $\varepsilon_{xx} \approx \varepsilon_{yy} \approx 15.49$ and $\varepsilon_{zz} \approx 17.49$, yielding an average value of

$$\langle \varepsilon_\infty \rangle = 16.16.$$

This suggests a moderate degree of dielectric anisotropy, with a slightly enhanced polarizability along the z-direction. Such behavior is typically associated with anisotropic bonding or structural asymmetry along this axis.

The electronic contribution to the dielectric tensor calculated using DFPT method yields slightly lower values, with an average of

$$\left\langle \varepsilon_\infty^{\mathrm{DFPT}} \right\rangle = 14.99,$$

while preserving the same anisotropic trend ($\varepsilon_{zz} > \varepsilon_{xx}, \varepsilon_{yy}$). The small discrepancy (~7–8%) between LOPTICS and DFPT results is not uncommon and can arise from differences in numerical settings, k-point sampling, or the treatment of local field effects. Nevertheless, the overall agreement confirms the reliability of the computed electronic dielectric response.

A key feature of the present system is the substantial ionic contribution to the dielectric screening. The ionic dielectric tensor ε_{ion} exhibits diagonal components on the order of ~16.7–17.4, with an average value of

$$\langle \varepsilon_{\text{ion}} \rangle = 16.93,$$

which is comparable in magnitude to the electronic part. This indicates strong lattice polarizability, typically associated with significant Born effective charges and/or soft infrared-active phonon modes. The comparable magnitudes of electronic and ionic contributions imply that lattice dynamics play a dominant role in the low-frequency dielectric response.

The total static dielectric tensor,

$$\varepsilon_s = \varepsilon_\infty + \varepsilon_{\text{ion}},$$

reaches values of $\varepsilon_{xx} \approx \varepsilon_{yy} \approx 31.03$ and $\varepsilon_{zz} \approx 33.72$, with an average value equal to

$$\langle \varepsilon_s \rangle = 31.93.$$

This relatively large static dielectric constant reflects the strong overall screening in the material. The difference between static and high-frequency limits,

$$\Delta\varepsilon = \varepsilon_s - \varepsilon_\infty \approx 15.77,$$

confirms that roughly half of the total dielectric response is due to ionic contributions, further emphasizing the importance of lattice polarization.

From a physical standpoint, the combination of (i) large ε_s, (ii) comparable electronic and ionic contributions, and (iii) weak but non-negligible anisotropy suggests that the material is a moderately polarizable dielectric with significant phonon-mediated screening. The slightly enhanced dielectric response along the z-direction may be linked to anisotropic bonding or vibrational modes, which can be further analyzed via phonon dispersion or Born effective charge tensors.

Overall, these results indicate that the material is characterized by strong dielectric screening, moderate anisotropy, and a substantial lattice contribution, making it potentially relevant for applications where high permittivity and efficient charge screening are desirable.

The temperature-dependent Seebeck coefficients for both n-type and p-type Mg_3Sb_2 reveal a characteristic evolution consistent with narrow-gap semiconductors governed by the competition between extrinsic and intrinsic carrier populations. At lower temperatures, the Seebeck magnitude increases linearly with temperature for all carrier concentrations, following the expected behavior of a degenerate semiconductor where the entropy per carrier rises as the Fermi level shifts relative to the band edge. However, as the temperature increases further, the material transitions into the bipolar conduction regime, marked by a distinct maximum in the Seebeck coefficient before a rapid decline occurs. This "bipolar hump" is created by the thermal excitation of minority carriers on the other side the bandgap, which contribute to the total thermoelectric power with the opposite sign and ultimately lead to a partial cancelation of the Seebeck voltage.

The position of this peak is highly sensitive to the initial carrier concentration, shifting systematically toward higher temperatures as the doping level increases. For the lowest carrier concentrations near 10^{15} cm^{-3}, the onset of intrinsic behavior is observed already at 400 K, whereas for the most heavily doped samples near 8.3×10^{18} cm^{-3}, the bipolar degradation is successfully suppressed until approximately 900 K. This suppression is critical for high-temperature thermoelectric applications, as it preserves the high Seebeck

magnitude required for a competitive figure of merit. In the n-type regime, the peak Seebeck values remain surprisingly high, exceeding 350 μV/K at optimal doping levels, which suggests a high degree of band degeneracy and a high effective mass density of states near the conduction band minimum.

In contrast, the p-type curves show a clear intersection of signs at high temperatures for lower doping ranges, reflecting an asymmetry in carrier mobilities or effective masses between the valence and conduction bands. As the system approaches the fully intrinsic limit above 1000 K, the curves for different doping levels converge, indicating that thermally generated carriers have become the dominant species, making the initial native defect concentrations negligible. The strong Seebeck response over the entire intermediate temperature range, especially for carrier concentrations of 10^{18} cm^{-3} range, highlights the potential of native defect engineering to stabilize Mg_3Sb_2 as a high-performance thermoelectric material. These results suggest that by carefully controlling the stoichiometry to favor specific native defects, the Fermi level can be effectively tuned to take advantage of the high-power factors provided by the electronic structure while delaying the detrimental effects of bipolar transport. The results obtained in this work show very good agreement with those reported by Shi et al. [35] for the Seebeck coefficient of n-type Mg_3Sb_2. In their study, at 700 K the Seebeck coefficient decreases from 400 μV/K to 200 μV/K as the electron carrier concentration increases from 0.1×10^{20} to 1×10^{20} cm^{-3}. A similar trend is observed at 300 K, where the Seebeck coefficient decreases from 300 to 200 μV/K with increasing n-type carrier concentration in the same range.

The temperature-dependent electrical conductivity for Mg_3Sb_2 reveals a distinct transition from extrinsic, defect-dominated transport to intrinsic semiconducting behavior. For the highest carrier concentrations, the conductivity follows a power-law decrease with increasing temperature, falling from approximately 8.5×10^4 S/m at room temperature to 3.45×10^4 S/m at 800 K. This trend indicates a degenerate semiconductor in which the Fermi level is located deep within the band, and carrier transport is limited mainly by acoustic phonon scattering. The ability of the material to maintain conductivity values within this range at elevated temperatures is a direct consequence of the strong degeneration of the conduction band. This electronic structure allows for maintaining high carrier densities without the drastic degradation of mobility typical of simpler single-valley semiconductors.

At lower carrier concentrations, the conductivity curves show a characteristic minimum followed by a sharp exponential increase at high temperatures. This "upturn" signifies the onset of intrinsic carrier excitation, where thermal energy becomes sufficient to move electrons across the bandgap. In this regime, the rapid increase in the population of both electrons and holes overwhelms the reduction in mobility caused by phonon scattering, leading to an increase in the total electrical conductivity. The temperature at which this transition occurs is highly sensitive to the initial carrier concentration induced by the defect, with samples with lower impurity content entering the intrinsic regime already at 500 K.

The convergence of all conductivity curves at temperatures exceeding 900 K underscores the intrinsic limit of the Mg_3Sb_2 lattice. At these thermal energies, the concentration of thermally generated carriers becomes the dominant transport factor, making the influence of specific native defect concentrations negligible. Furthermore, the p-type conductivity generally maintains higher absolute values than the n-type for equivalent lower-temperature carrier concentrations, suggesting an asymmetry in the effective mass or scattering physics between the valence and conduction bands. Overall, these results demonstrate that managing native defect chemistry to favor higher carrier densities effectively delays the onset of bipolar conduction, allowing the material to maintain the high electrical conductivity necessary for efficient thermoelectric performance at high temperatures.

The results obtained in this work are in good agreement with the electrical conductivity of Mg_3Sb_2 recently reported by Li et al. [36]. However, it should be noted that the conductivity in their study was measured for doped Mg_3Sb_2. In contrast, the calculations presented here correspond to specific carrier concentrations, which makes the comparison reasonable, as the primary effect of doping is the introduction of charge carriers into the pristine material. The experimental data for the Seebeck coefficient and electrical conductivity are not included in Figures 4 and 5, because those measurements were performed on doped samples rather than on Mg_3Sb_2 with intrinsic carrier concentrations.

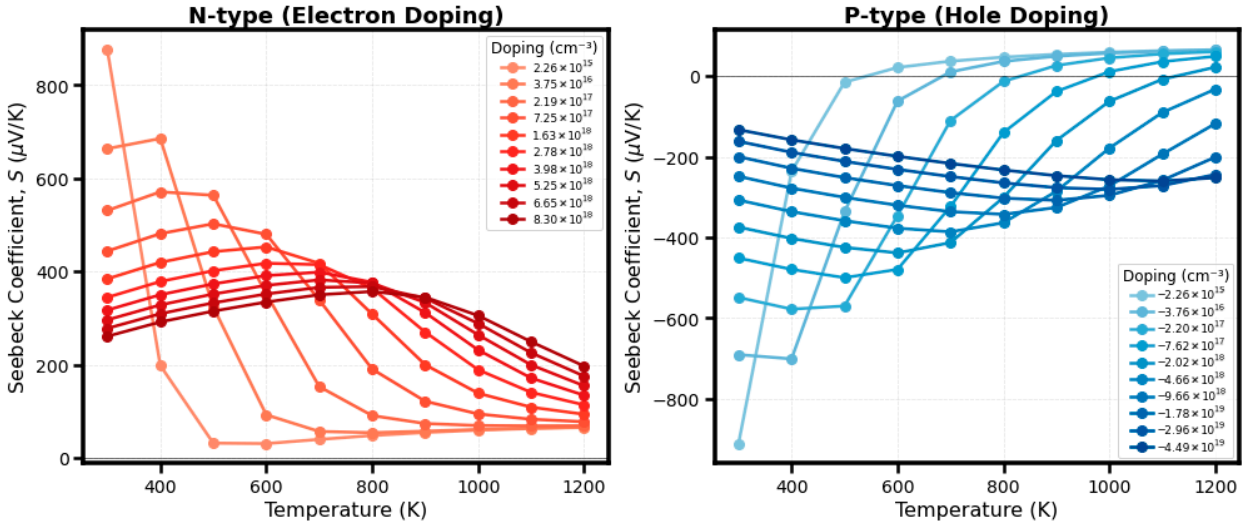

Figure 4. Seebeck coefficient for various carrier concentration in temperature range 300–200 K for n-type Mg_3Sb_2 (**left**) and p-type Mg_3Sb_2 (**right**).

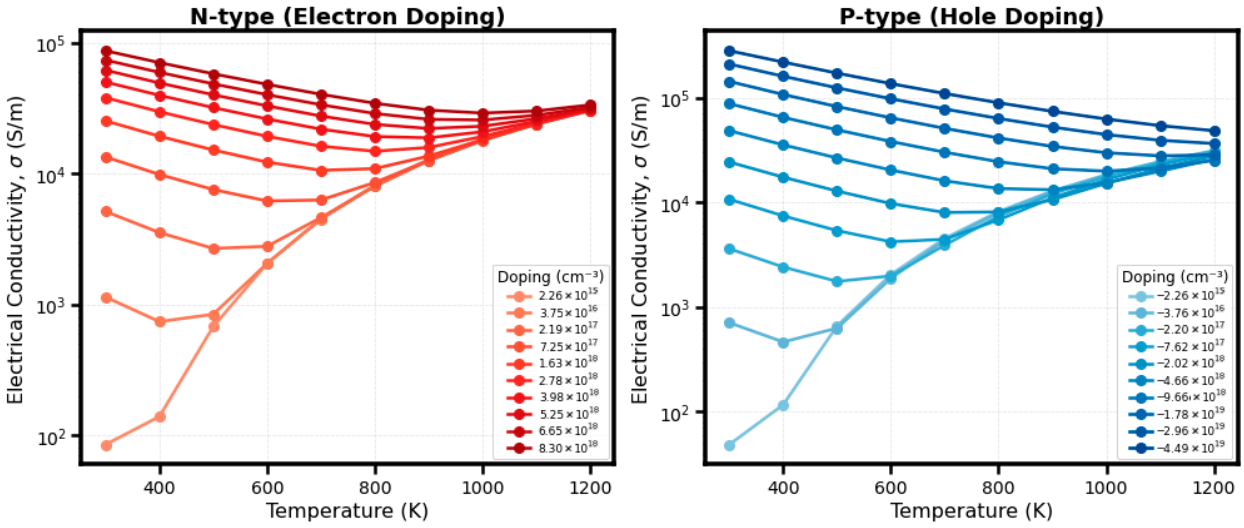

Figure 5. Electrical conductivity for various carrier concentration in the temperature range 300–200 K for n-type Mg_3Sb_2 (**left**) and p-type Mg_3Sb_2 (**right**).

As mentioned earlier, the calculation of lattice thermal conductivity requires second- and third-order interatomic force constants (IFCs), which were obtained using Phonopy [24] and Phono3py [24], respectively. Although both second- and third-order IFCs can be calculated using Phono3py [24] alone, the approach adopted in this work allows for cross-validation of the results, which is particularly valuable given the large difference in computational effort required to obtain the force sets.

Phonopy [24] required only five supercells to compute the second-order IFCs, whereas Phono3py [24] required 375 supercells for the third-order IFCs, assuming a cutoff radius of 5 Å. This cutoff was selected as an optimal compromise between computational cost and accuracy. It is evident that, if inappropriate input parameters were used without prior verification, significant computational resources could be wasted.

The phonon dispersion curves of Mg_3Sb_2 obtained using Phonopy [24] are presented in Figure 6 along with data given by Lee et al. [37].

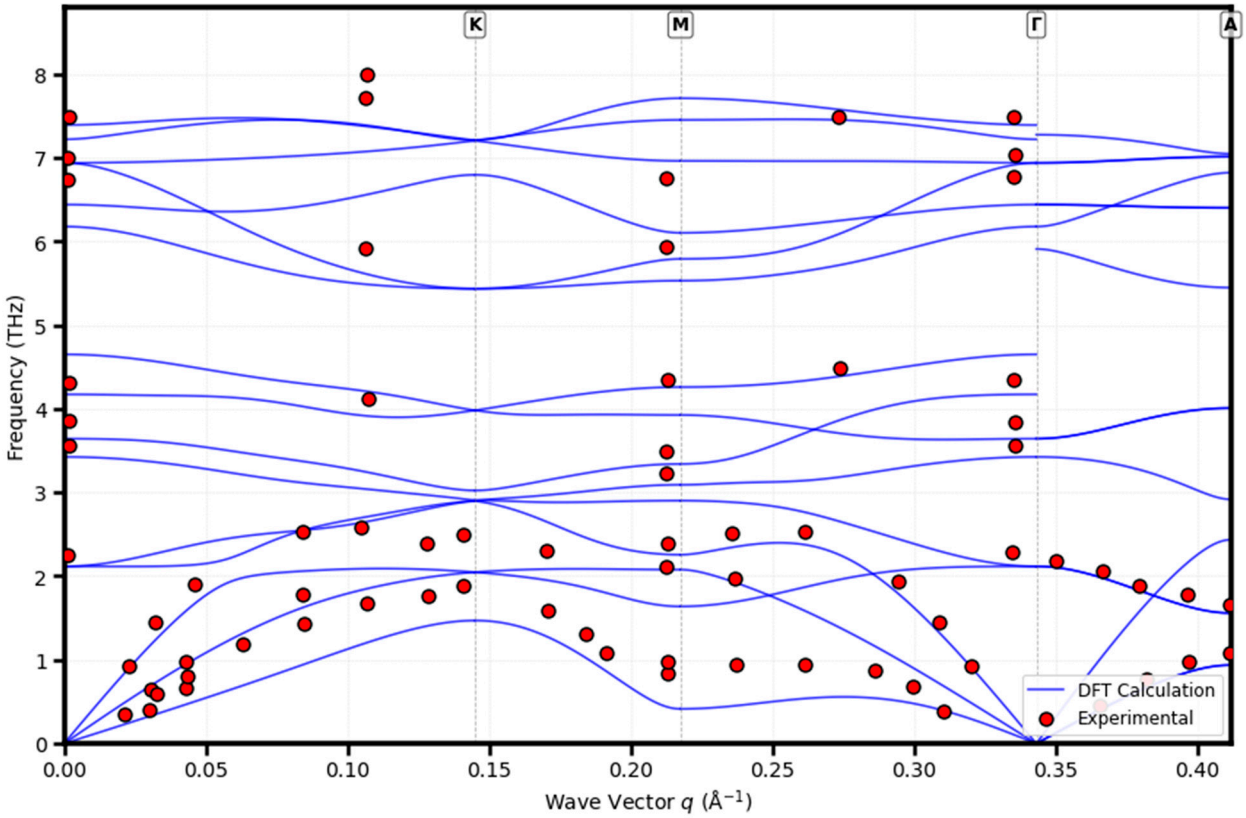

Figure 6. Phonon dispersion curves of the Mg_3Sb_2 compared with experimental data given by Lee et al. adapted from [37].

The phonon dispersion relations, calculated along the high-symmetry directions of the Brillouin zone, provide fundamental insight into the lattice dynamics and the intrinsic origins of the low lattice thermal conductivity in this Zintl phase. The spectrum is characterized by three acoustic branches—one longitudinal and two transverse—which are confined to a narrow frequency range below 2.5 THz. The relatively shallow slopes of these acoustic modes, particularly the transverse branches, indicate low phonon group velocities, which directly contributes to the suppression of thermal transport. Above 3 THz a dense manifold of optical branches is observed, exhibiting a significant flatness across the Brillouin zone. These flat optical modes represent vibrational states with group velocities close to zero, which do not transfer heat effectively but serve as important scattering channels for acoustic phonons via anharmonic Umklapp processes [38].

The calculated dispersion curves show excellent agreement with the experimental data, conforming the accuracy of the interatomic force constants and the exchange-correlation functional used in the simulations. A significant overlap between the acoustic and the lowest-lying optical branches occurs near 2.5 THz, creating a high density of states that facilitates strong acoustic–optical phonon coupling. This interaction typically leads to enhanced scattering rates, further reducing the phonon mean free path. The dynamical

stability of the crystal structure is confirmed by the complete absence of imaginary frequencies along the entire wave vector path. Furthermore, the distinct vibrational characteristics along the paths highlight the structural anisotropy inherent to the hexagonal lattice, which influences the directional dependence of the lattice thermal conductivity. Collectively, these vibrational properties provide the physical foundation for the exceptionally low thermal conductivity lattice, necessary to achieve the high thermoelectric figure of merit reported in this study. Figure 6 also presents the experimental determination of phonons in the Mg_3Sb_2 phase reported by Lee et al. [37]. It is obvious that the calculations presented in this work are in good agreement with the experimental determinations.

Having calculated phonons as well as the second order of IFCs, it was possible to calculate the third order of IFCs, and, in consequence, the thermal lattice conductivity that is equal to 1.3125 W/mK.

The previous step completed the set of parameters required to calculate the thermoelectric figure of merit ZT according to Equation (21). Figure 7 presents the results obtained in this work for pristine Mg_3Sb_2, including intrinsic defects in the crystal structure.

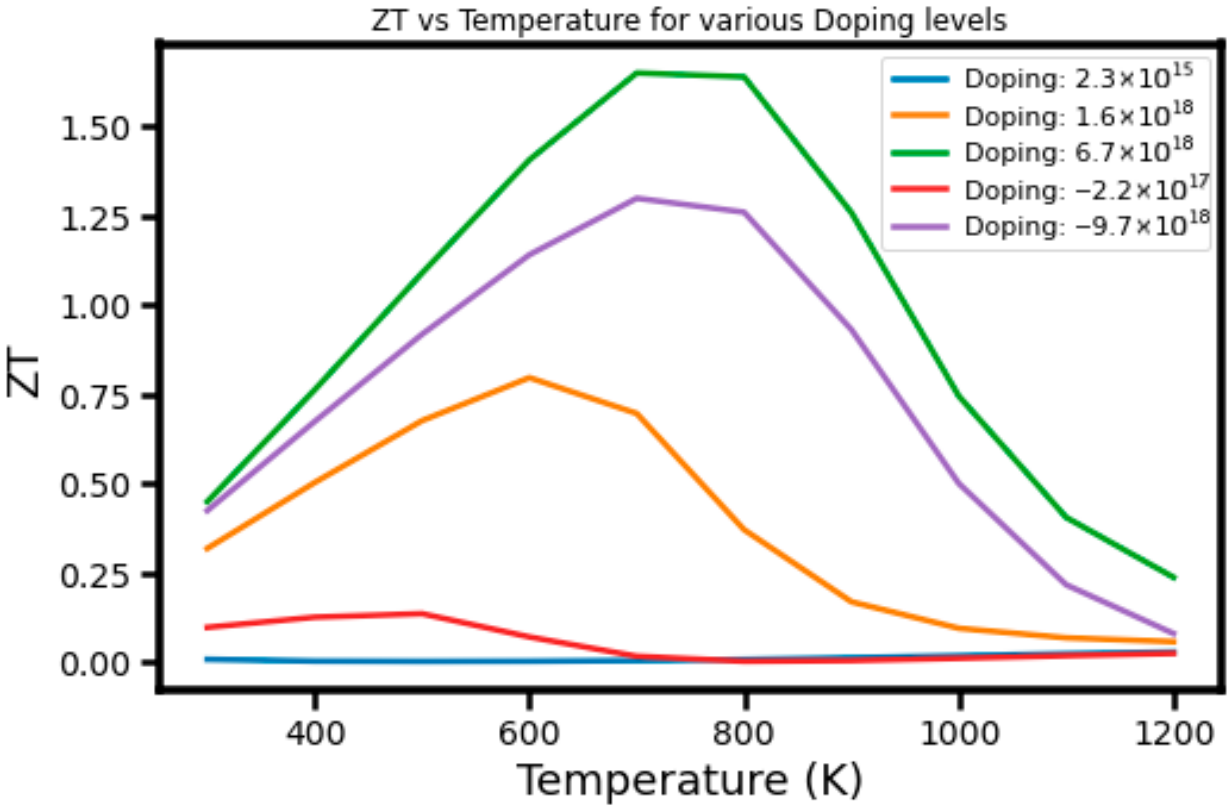

Figure 7. The thermoelectric figure of merit zT as a function of doping and temperature.

The temperature-dependent figure of merit (zT) highlights the critical role of tuning the carrier concentration via native defects in achieving high thermoelectric efficiency. The results demonstrate a clear evolution from negligible values in nearly intrinsic samples to exceptional values exceeding 1.5 in heavily doped regimes. For the lowest carrier concentrations (2.3×10^{15} cm^{-3}), it remains close to zero over the entire temperature range, because the material is characterized by low electrical conductivity and early onset of bipolar thermal conduction, which leads to the mutual cancelation of the Seebeck coefficient.

As the concentration of native defects increases, the peaks shift systematically towards higher temperatures. For optimized n-type doping (6.7×10^{18} cm^{-3}), the curve reaches a maximum of about 1.65 at temperatures between 700 K and 800 K. This peak is the result of a synergistic balance where the high electrical conductivity and Seebeck coefficient are

maintained, while the bipolar effect is effectively delayed to higher thermal energies. In the p-type regime (9.7×10^{18} cm^{-3}), the material also shows high efficiency with a peak around 1.3. The slightly lower efficiency in p-type compared to n-type is attributed to differences in the band structure, specifically the greater valley degeneracy in the conduction band that favors n-type transport.

The rapid degradation observed above 800 K for all doping levels indicates the temperature at which the excitation of intrinsic carrier becomes dominant. Within this high-temperature limit, minority carriers' proliferation increases the total thermal conductivity via the bipolar contribution while simultaneously reducing the Seebeck voltage, leading to a sharp drop in the overall efficiency. These results confirm that it is a top-class thermoelectric material when native defects are engineered to achieve carrier densities in the range of 10^{18} to 10^{19} cm^{-3}. By establishing this theoretical ceiling for pure phases, the data underscores that high thermoelectric efficiency is an intrinsic property of the electronic and vibrational structure of the Zintl phase, provided that the stoichiometry is precisely controlled to suppress detrimental intrinsic excitations.

4. Conclusions

A comprehensive, first-principles investigation of charged point defects in the Mg_3Sb_2 system was performed using density functional theory (DFT) within the generalized gradient approximation (GGA). Defect formation energies and phase transitions were calculated to elucidate the fundamental electronic and structural properties of native defects. It was found that, depending on the chemical potential, vacancies and antisites emerge as the dominant defect species, and deep transition levels are introduced within the fundamental band gap.

The intrinsic carrier concentrations and conductivity types were mapped across various thermal regimes through a self-consistent determination of the Fermi level, providing insights into self-compensation and defect-controlled doping mechanisms. Furthermore, the thermoelectric transport properties—including the Seebeck coefficient, electrical conductivity, and electronic thermal conductivity—were evaluated using Boltzmann transport theory. A strong correlation was observed between the defect-induced Fermi level pinning and the resulting power factor, suggesting that optimal figure of merit (zT) values are restricted by spontaneous compensation in specific chemical potential regimes. Ultimately, it was demonstrated how modeling and defect engineering can be leveraged to map phase boundaries and optimize the thermoelectric performance of Mg_3Sb_2-based materials.

Author Contributions: M.B.: Writing—original draft, Investigation, Conceptualization, Data curation. A.D.: Resources, Writing—review and editing. W.G. (Władysław Gąsior): Resources, Writing—review and editing. W.G. (Wojciech Gierlotka): Project administration, Supervision, Investigation, Writing—review and editing, Funding acquisition. All authors have read and agreed to the published version of the manuscript.

Funding: The work was supported by the Science and Technology Council, Taiwan (R.O.C.) under grant 114-2221-E-259-009.

Data Availability Statement: The original contributions presented in the study are included in the article, further inquiries can be directed to the corresponding author.

Acknowledgments: We gratefully acknowledge the Polish high-performance computing infrastructure PLGrid (HPC Center: ACK Cyfronet AGH) for providing computer facilities and support within the computational grant no. PLG/2024/017843.

Conflicts of Interest: The authors declare no conflict of interest.

References

1. Zhao, D.; Tan, G. A review of thermoelectric cooling: Materials, modeling and applications. *Appl. Therm. Eng.* **2014**, *66*, 15–24. [CrossRef]
2. Li, A.; Fu, C.; Zhao, X.; Zhu, T. High-Performance Mg_3Sb_2-xBix Thermoelectrics: Progress and Perspective. *Research* **2020**, *2020*, 1934848. [CrossRef]
3. Bhardwaj, A.; Rajput, A.; Shukla, K.; Pulikkotil, J.J.; Srivastava, A.K.; Dhar, A.; Gupta, G.; Auluck, S.; Misra, D.K.; Budhani, R.C. Mg_3Sb_2-based Zintl compound: A non-toxic, inexpensive and abundant thermoelectric material for power generation. *R. Soc. Chem.* **2013**, *3*, 8504–8516. [CrossRef]
4. Weber, E.R.; Schneider, J. AsGa antisite defects in GaAs. *Phys. B+C* **1983**, *116*, 398–403. [CrossRef]
5. Zhilinskaya, E.A.; Valeev, N.k.; Oblasov, A.K. Ge_xS_{1-x} glasses. II. Synthesis conditions and defect formation. *J. Non-Cryst. Solids* **1992**, *146*, 285–293. [CrossRef]
6. Zhou, W.; Greer, H.F. What Can Electron Microscopy Tell Us Beyond Crystal Structures? *Eur. J. Inorg. Chem.* **2016**, *2016*, 941–950. [CrossRef]
7. Sosnowska, I.M.; Shiojiri, M. Oxides: Neutron and synchrotron X-ray diffraction studies. *J. Electron Microsc.* **1999**, *48*, 681–687. [CrossRef]
8. Mohammed, M.H.; Hanoon, F.H. First-principles study on the physical properties for various anticancer drugs using density functional theory (DFT). *Solid State Commun.* **2021**, *325*, 114160. [CrossRef]
9. Liu, C.-Y.; Liu, Y.-Y.; Chen, S.-H.; Chen, S.-W.; Dębski, A.; Gąsior, W.; Gielotka, W. Thermodynamic modeling of the Sb–Te system supported by DSC measurement and ab initio calculations. *J. Mater. Res.* **2023**, *38*, 4287. [CrossRef]
10. Wang, L.; Zhang, W.; Back, S.Y.; Kawamoto, N.; Mori, T. High-performance Mg_3Sb_2-based thermoelectrics with reduced structural disorder and microstructure evolution. *Nat. Commun.* **2024**, *15*, 6800.
11. Mohanty, S.; Basu, R.; Panther, A.; Rai, A.K.; Basu, H.; Singh, A. Optimizing the Excess Mg in n-Type Mg_3Sb_2 Alloy: An Alternate Material Toward Sustainable Thermoelectric Conversion at Room Temperature. *ChemNanoMat* **2026**, *12*, e202500638.
12. Liang, Z.; Jian, M.; Xu, C.; Lei, B.-H.; Shang, H.S.; Ren, W.; Ding, F.; Singh, D.J.; Feng, Z.; Ren, Z. Intrinsic thermal stability enhancement in n-type Mg_3Sb_2 thermoelectrics toward practical applications. *Acta Mater.* **2023**, *247*, 118752.
13. Kresse, G.; Hafner, J. Ab initio molecular dynamics for liquid metals. *Phys. Rev. B* **1993**, *47*, 558.
14. Perdew, J.P.; Burke, K.; Ernzerhof, M. Generalized Gradient Approximation Made Simple. *Phys. Rev. Lett.* **1996**, *78*, 1396. [CrossRef]
15. Kavanagh, S.R.; Squires, A.G.; Nicolson, A.; Mosquera-Lois, I.; Ganose, A.M.; Zhu, B.; Brlec, K.; Walsh, A.; Scanlon, D.O. doped: Python toolkit for robust and repeatable charged defect supercell calculations. *J. Open Source Softw.* **2024**, *9*, 6433. [CrossRef]
16. Sze, S.M.; Ng, K.K. *Physics of Semiconductor Devices*; Wiley: Hoboken, NJ, USA, 2021.
17. Voigt, W. Wechselbeziehungen zwischen einem Vektor und einem Tensortripel. In *Lehrbuch der Kristallphysik*; Teubner: Leipzig, Germany, 1928; pp. 801–944.
18. Ganose, A.M.; Park, J.; Faghaninia, A.; Woods-Robinson, R.; Persson, K.A.; Jain, A. Efficient calculation of carrier scattering rates from first principles. *Nat. Commun.* **2021**, *2*, 2222. [CrossRef]
19. Nielsen, O.H.; Martin, R.M. First-principle calculations of stress. *Phys. Rev. Lett.* **1983**, *50*, 697–700. [CrossRef]
20. Reuss, A.; Angnew, Z. A calculation of the bulk modulus of polycrystalline materials. *Math Meth* **1929**, *9*, 55.
21. Chen, X.-Q.; Niu, H.; Li, D.; Li, Y. Modeling Hardness of Polycrystalline Materials and Bulk Metallic Glasses. *Intermetallics* **2011**, *19*, 1275–1281. [CrossRef]
22. Tian, Y.-J.; Xu, B.; Zhao, Z. First-Principles Calculations of the Structural, Mechanical and Thermodynamics Properties of Cubic Zirconia. *J. Refract. Met. Hard Mater.* **2012**, *33*, 93–106.
23. Gierlotka, W.; Debski, A.; Terlicka, S.; Gasior, W.; Peska, M.; Polanski, M. Insight into Phase Stability in the Mg-Pd System: The Ab Initio Calculations. *J. Phase Equilibria Diffus.* **2020**, *41*, 681–686.
24. Togo, A. First-principles Phonon Calculations with Phonopy and Phono3py. *J. Phys. Soc. Jpn.* **2023**, *92*, 012001. [CrossRef]
25. Horton, M.K.; Huck, P.; Yang, R.X.; Munro, J.M.; Dwaraknath, S.; Ganose, A.M.; Kingsbury, R.S.; Wen, M.; Shen, J.X.; Mathis, T.S.; et al. Accelerated data-driven materials science with the Materials Project. *Nat. Mater.* **2025**, *24*, 1522–1532. [CrossRef] [PubMed]
26. Jain, A.; Ong, S.P.; Hautier, G.; Chen, W.; Richards, W.D.; Dacek, S.; Cholia, S.; Gunter, D.; Ceder, G.; Persson, K.A. Commentary: The Materials Project: A materials genome approach to accelerating materials innovation Free. *APL Mater.* **2013**, *1*, 011002. [CrossRef]
27. Saal, J.E.; Kirklin, S.; Aykol, M.; Meredig, B.; Wolverton, C. Materials Design and Discovery with High-Throughput Density Functional Theory: The Open Quantum Materials Database (OQMD). *Springer Nat. Link.* **2013**, *65*, 1501–1509. [CrossRef]
28. Kirklin, S.; Saal, J.E.; Meredig, B.; Thompson, A.; Doak, J.W.; Aykol, M.; Rühl, S.; Wolverton, C. The Open Quantum Materials Database (OQMD): Assessing the accuracy of DFT formation energies. *npj Comput. Mater.* **2015**, *1*, 15010. [CrossRef]
29. Zintl, E.; Husemann, E. Bindungsart und Gitterbau binärer Magnesiumverbindungen. *Phys. Sci.* **2017**, *21*, 138–155. [CrossRef]

30. Li, H.; Li, J.; Newton, M.A.A.; Yu, J.; Chen, C.; He, Z.; Chen, L.; Wang, Z.; Huang, Z.; Hayashi, K.; et al. A critical review of Mg_3Sb_2-based thermoelectric materials. *Appl. Phys. Express* **2026**, *19*, 020101. [CrossRef]
31. Owais, M.; Luo, X.; Huang, B.; Yang, Y.; Rehman, M.; Mushtaq, R.T. Enhancing Thermoelectric Performance of Mg_3Sb_2 Through Substitutional Doping: Sustainable Energy Solutions via First-Principles Calculations. *MDPI-Energ.* **2024**, *17*, 5358. [CrossRef]
32. Mosquera-Lois, I.; Kavanagh, S.R.; Walsh, A.; Scanlon, D.O. ShakeNBreak: Navigating the defect configurational landscape. *J. Open Source Softw.* **2022**, *7*, 4. [CrossRef]
33. Ohno, S.; Imasato, K.; Anand, S.; Tamaki, H.; Kang, S.; Gorai, P.; Sato, H.; Toberer, E.; Kanno, T.; Snyder, G. Phase Boundary Mapping to Obtain n-type Mg_3Sb_2-Based Thermoelectrics. *Joule-A Cell Press J.* **2018**, *2*, 141–154. [CrossRef]
34. Curtarolo, S.; Kolmogorov, A.N.; Cocks, F.H. High-throughput ab initio analysis of the Bi–In, Bi–Mg, Bi–Sb, In–Mg, In–Sb, and Mg–Sb systems. *Calphad* **2005**, *29*, 155–161. [CrossRef]
35. Shi, X.; Zhao, T.; Zhang, X.; Sun, C. Extraordinary n-Type Mg_3 SbBi Thermoelectrics Enabled by Yttrium Doping. *Adv. Mater.* **2019**, *31*, 1903387.
36. Li, J.; Liu, K.; Ma, X.; Yang, Z.; Yi, L.; Mao, J.; Zhang, Q. Improvement of the Thermoelectric Properties of p-Type Mg_3Sb_2 by Mg-Site Double Substitution. *Inorg. Chem.* **2024**, *63*, 20126–20132. [CrossRef]
37. Lee, C.H.; Kunioka, H.; Mori, H.; Hasegawa, T. Phonon dynamics on thermoelectric material of Mg_3Sb_2. *Act. Rep. Neutron Scatt. Res. Exp. Rep.* **2018**, *24*, 1903.
38. Han, Y.-J. Intrinsic thermal-resistive process of crystals: Umklapp processes at low and high temperatures. *Phys. Rev. B* **1996**, *54*, 8977. [CrossRef]

Disclaimer/Publisher's Note: The statements, opinions and data contained in all publications are solely those of the individual author(s) and contributor(s) and not of MDPI and/or the editor(s). MDPI and/or the editor(s) disclaim responsibility for any injury to people or property resulting from any ideas, methods, instructions or products referred to in the content.